Analysis and design of lattice materials for large cord and curvature variations in skin panels of morphing wings

2015 Smart Mater. Struct. 24 037006

(http://iopscience.iop.org/0964-1726/24/3/037006)

IOP Publishing Smart Materials and Structures
Smart Mater. Struct. **24** (2015) 037006 (11pp) doi:10.1088/0964-1726/24/3/037006

Technical Note

Analysis and design of lattice materials for large cord and curvature variations in skin panels of morphing wings

Andrea Vigliotti[1] **and Damiano Pasini**[2]

[1] Department of Engineering, University of Cambridge, Trumpington Street, Cambridge CB2 1PZ, UK
[2] Department of Mechanical Engineering, McGill University, 845 Sherbrooke St. W, Montreal H3A 2T5, Canada

E-mail: av388@cam.ac.uk and damiano.pasini@mcgill.ca

Received 13 October 2014, revised 18 December 2014
Accepted for publication 22 December 2014
Published 13 February 2015

Abstract

In the past few decades, several concepts for morphing wings have been proposed with the aim of improving the structural and aerodynamic performance of conventional aircraft wings. One of the most interesting challenges in the design of a morphing wing is represented by the skin, which needs to meet specific deformation requirements. In particular when morphing involves changes of cord or curvature, the skin is required to undergo large recoverable deformation in the actuation direction, while maintaining the desired shape and strength in the others. One promising material concept that can meet these specifications is represented by lattice materials. This paper examines the use of alternative planar lattices in the embodiment of a skin panel for cord and camber morphing of an aircraft wing. We use a structural homogenization scheme capable of capturing large geometric nonlinearity, to examine the structural performance of lattice skin concepts, as well as to tune their mechanical properties in desired directions.

Keywords: morphing structures, lattice materials, nonlinear mechanics, multiscale mechanics, adaptive structures

(Some figures may appear in colour only in the online journal)

1. Introduction

With the aim of improving the performance and the efficiency of current aircraft design, various concepts for wing morphing have been recently proposed. Compared to conventional wing designs, the benefits of a morphing wing include improved aerodynamic efficiency, along with reduced structural weight and noise emission (Wlezien *et al* 1998, Stanewsky 2001). Morphing components are currently used in unmanned aerial vehicles (Gomez and Garcia 2011) and advanced wind turbine blades (Daynes and Weaver 2012), where aerodynamic efficiency is critical. In general, they are amenable in sectors subjected to a softer regulation, as opposed to manned flight, and in applications open to foster new solutions. Given the number and the diversity of approaches described in literature, no attempt is made here to summarize them; yet, we point the interested readers to thorough reviews on the subject (Sofla *et al* 2010, Barbarino *et al* 2011, 2014, Kuder *et al* 2013).

In this introduction, we limit ourselves to mention some recent studies that develop or apply strategies relevant to the method used in this paper. For example, (Santer and Pellegrino 2009) used a load path-based topology optimization technique to design the internal structure of a compliant wing leading edge. Previtali and Ermanni (2012) introduced a method that uses the wing eigenmodes for the optimal design of a morphing wing. A number of other studies focused on controlling compliance in the wing cores. For twist morphing, (Raither *et al* 2013) proposed to tune the shear stiffness of the wing box with temperature changes that in turn control the

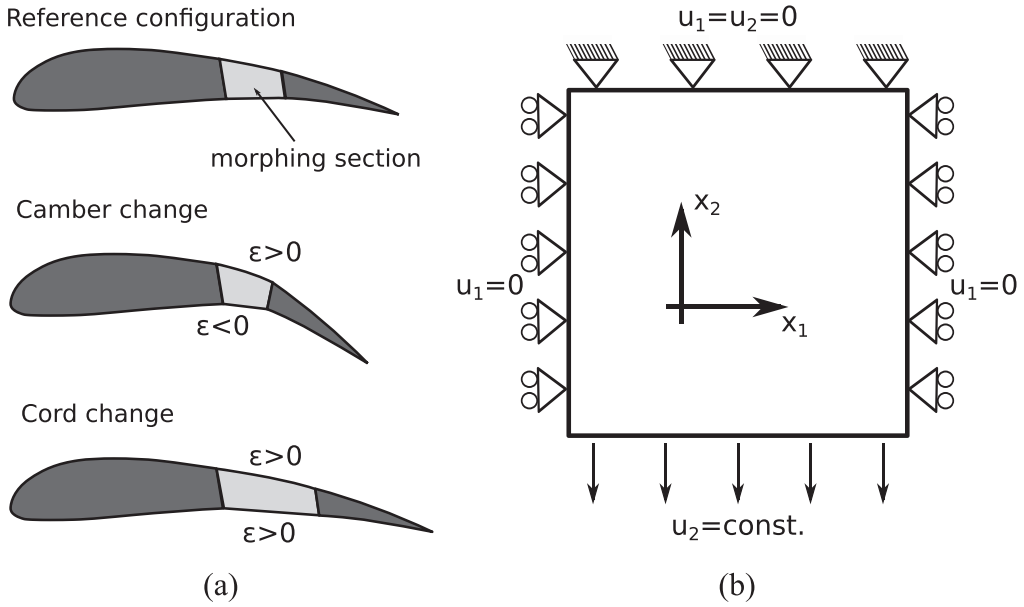

Figure 1. (a) Camber and cord variation achieved via wing morphing. (b) Reference boundary conditions are imposed to determine the skin material properties.

modulus properties of hard polyvinyl chloride. Spadoni and Ruzzene (2007) explored the potential of a chiral core aerofoil for a variable camber morphing wing. Other recent studies have specifically focused on the design of the wing skin, with a good review of such efforts available from Thill *et al* (2008). The skin of morphing wings poses some interesting design challenges. With reference to figure 1(a), when large variations in cord or curvature are required, the skin should be able to provide high compliance in the wing plane as well as exhibit high stiffness and strength in the out of plane direction, so as to maintain the required shape under the action of the aerodynamic loads. In addition, the high compliance of the skin is desirable to limit the power and the mass of the actuators (Wereley and Gandhi 2010). Powered by recent technologies that allow the accurate manufacturing of repetitive microstructures at a very small scale (Ortona *et al* 2012, Vaezi *et al* 2013, Hengsbach and Lantada 2014), lattice materials have been often flagged as a promising design solution for morphing applications. For example, (Olympio *et al* 2010, Olympio and Gandhi 2010a, 2010b) evaluated the elastic properties of skin panels with various micro-architectures of the cellular core. Thill and others (Thill *et al* 2010) suggested the use of a corrugated composite panel for the design of a morphing trailing edge. Corrugated cores as a support for highly deformable elastomeric skin have also been studied by (Dayyani *et al* 2014). Chen *et al* (2013) designed and tested a fibre reinforced flexible skin with highly auxetic behaviour.

In most of the works cited above, a particular attention is given to design solutions involving materials with a lattice architecture. The properties of cellular materials have been described in detail, mainly with closed-form expressions, by Gibson *et al* (1982), Gibson and Ashby (1982). More recently, numeric homogenization techniques have been proposed to accurately study the mechanics of lattice materials (Arabnejad and Pasini 2013). In this paper, a numeric multiscale scheme capable to capture the geometric nonlinearity of an architectured medium is used to derive the macroscopic constitutive relationships of a morphing skin made of a lattice. From the analysis of a representative volume element (RVE) subjected to a given macroscopic deformation field and periodic boundary conditions, the components of the stress field are obtained and assigned to a homogeneous uniform material which has deformation work equivalent to that of the lattice. The method is here applied to appraise and compare the skin performance of alternative lattice topologies for wing skin morphing.

2. Material requirements for the skin of morphing wings with large curvature and cord variations

This section describes the material requirements to design a skin panel for a morphing wing. We first emphasize that alternative approaches exist to achieve wing morphing, each tailored to meet specific aspects, such as global wing configuration, attitude or lift control, each with specific requirements for the materials. This paper focuses on lift control solutions that require large variations of the cord and the curvature of the airfoil. As a reference, figure 1(a), we examine a rectangular flapless wing, whose camber and cord are controlled by the morphing of the trailing edge. In this configuration, the aerofoil skin must essentially undergo membrane deformation in the skin-plane, and withstand the aerodynamic pressure in the out of plane direction. For cord changes, the upper and lower surfaces generally undergo deformation of identical sign, whereas for camber changes, the surface deformation has opposite sign. This regime imposes the skin to withstand both large tensile and compressive recoverable deformations. In addition, we note that

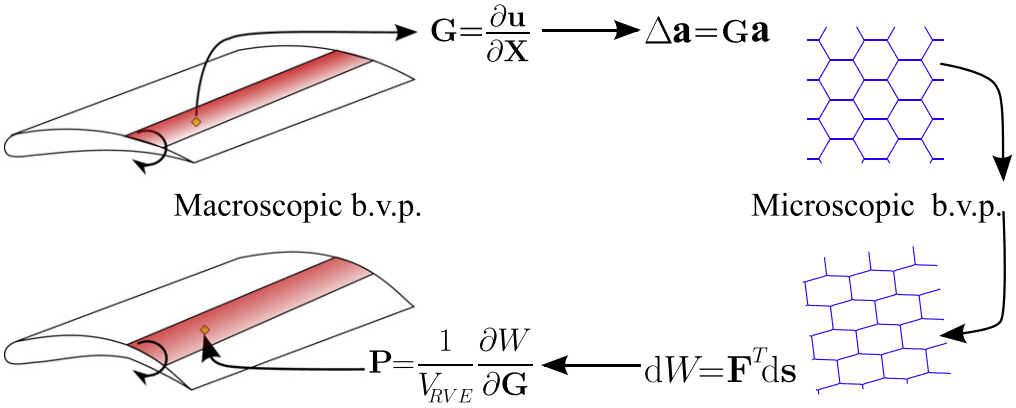

Figure 2. Multiscale scheme. At every integration point of the macroscopic model, the first Piola–Kirchoff tensor, **P**, is evaluated—via a finite element model of the RVE—as a function of the macroscopic displacement gradient, **G**, after periodic boundary conditions are imposed on the RVE.

shape changes are controlled by actuators usually installed in the wing body. To reduce both the power requirements and the impact of the actuation forces on the rest of the wing structure, the skin material is required to be very compliant in the direction of actuation. Another requirement is that throughout the actuation the skin should exhibit low in-plane Poissons ratio, a behaviour that reduces the loads transmitted in the transverse directions to the rest of the wing. In summary, the material specifications for the skin design of a morphing wing that aims at achieving large variation of cord or curvature can be abridged as follows:

(1) high macroscopic in plane compliance in the direction of actuation to minimize actuator's power and overall structural mass of the wing;
(2) large recoverable macroscopic elastic deformation to allow the shape changes required by the aerodynamics;
(3) zero in plane Poisson's ratio to ensure that no undesired forces are generated in the span-wise direction and to reduce the overall structural mass of the wing;
(4) high bending stiffness to ensure no shape variation occurs under the action of the aerodynamic pressure;
(5) minimal structural mass of the skin panel.

The requirements listed above are generally in conflict for any homogeneous material and for ordinary composite materials. For example, a polymeric rubber, which is naturally very compliant, could satisfy criteria 1 and 2, but very likely it could not satisfy the other criteria. On the other hand, composite materials can provide a high level of anisotropy, but their tolerance to large deformation is quite limited. In this paper, we focus on the design of materials with lattice architecture for morphing skins. For a preliminary design, the first design step involves the selection of the topology class, either stretching or bending dominated (Deshpande *et al* 2001). The former is statically determinate in its pin-jointed version, and is capable to withstand any macroscopic load responding with axial forces in the struts. The latter, on the other hand, is statically indeterminate in its pin-jointed configuration, and thus presents modes in the lattice elements that are dominated by bending. The bending dominated lattice is macroscopically very compliant and can accommodate large macroscopic deformation at the expense of relatively small strain in the solid material. On the other hand, bending dominated lattices are comparatively very stiff and strong for the loads that produce axial forces in the elements. This shows that the macroscopic response of the material can be tuned by the proper selection of the cell topology and the lattice parameters. In principle, a lightweight lattice that is extremely stiff for some loading conditions, and compliant in others, can be tuned to undergo large macroscopic deformation fulfilling the entire set of requirements for a morphing skin.

3. Methodology

Components made out of lattice materials are characterized by a substructure obtained from the tessellation of a unit cell along independent periodic directions. If the scale of the component is significantly larger than the scale of the lattice, a direct approach involving the modelling of each cell is impractical. This strategy would result in considerably large models, which are likely to be unmanageable. An alternative is the substitution of the discrete model with an equivalent continuum (Noor 1988). At the cost of losing minor local details, we can obtain a substantial reduction of the computational effort with still accurate results. We adopt here a multiscale approach to predict macroscopic deformation response of a lattice. As illustrated in figure 2, the stiffness of the material at the macroscopic level can be determined by assuming that the lattice microstructure behaves as a uniform continuum. At the microscopic level, we first calculate the deformation energy of the lattice, and then use the virtual work principle to determine the components of the homogenized stress field. For solid materials, a functional relation is assumed between the stress and strain tensors. For lattice materials, since the response depends on the properties of the microstructure, this relation cannot be directly expressed as a functional dependence. In particular, for a material subjected

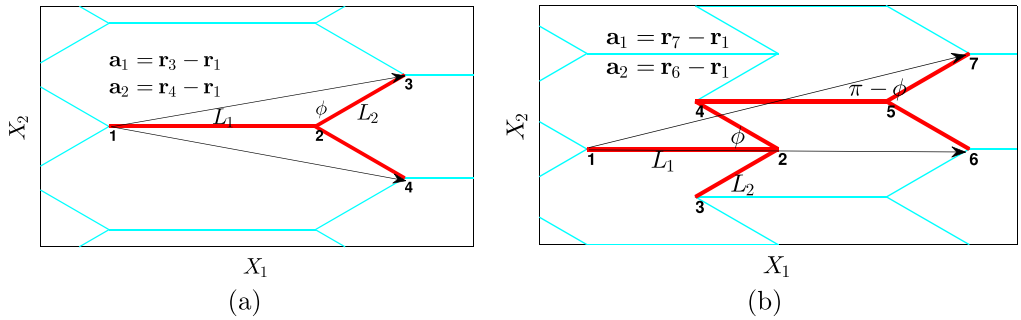

Figure 3. Sample topologies: (a) hexagonal lattice, (b) chevron lattice. The thick red lines represent the unit cell elements; $\mathbf{a}_1$ and $\mathbf{a}_2$ are the tessellation vectors; r_i is the coordinate vector of node i; L_1 and L_1 are respectively the length of the horizontal and inclined members; ϕ is the angle between the horizontal and the inclined members.

to large deformation emerging from microscale geometric nonlinearity, such relationship depends on the lattice configuration. Yet, we can formulate a boundary value problem to calculate the lattice strain energy, and to express it as a function of the macroscopic strain. The components of the macroscopic stress field are then obtained by differentiating the macroscopic strain energy with respect to the components of the macroscopic strain field. Hereafter, we briefly summarize the main aspects of the method, applied here to obtain the macroscopic constitutive relations for the in plane deformation of the skin. A complete description can be found in (Vigliotti and Pasini 2012a, 2012b, Vigliotti *et al* 2014).

Let us consider a finite element model of a RVE of the lattice, which is defined as the subset of structural elements that are capable to generate the entire lattice after replication along periodic directions. Let $\mathbf{s}$ be the array of the nodal degrees of freedom of the RVE, the corresponding array of the nodal forces, $\mathbf{F}(\mathbf{s})$, can be calculated by a finite element analysis of the RVE. The first order variation of the strain energy, due to a change of the macroscopic strain, can be obtained by applying the principle of the virtual work as follows

$$\mathrm{d}W = \int_{V_{\mathrm{RVE}}} P_{ij}\mathrm{d}G_{ij}\,\mathrm{d}V = \mathbf{F}^T\mathrm{d}\mathbf{s}. \tag{1}$$

In the above equation, P_{ij} and G_{ij} are respectively the components of the macroscopic first Piola–Kirchoff (1PK) stress tensor and of the macroscopic displacement gradient, $\mathrm{d}\mathbf{s}$ is the variation of the nodal displacements corresponding to $\mathrm{d}G_{ij}$. Assuming that P_{ij} and G_{ij} are uniform over the RVE, we obtain the following expression for the macroscopic stress tensor

$$P_{ij} = \frac{1}{V_{\mathrm{RVE}}}\frac{\partial W}{\partial G_{ij}} = \frac{1}{V_{\mathrm{RVE}}}\mathbf{F}^T\frac{\partial \mathbf{s}}{\partial G_{ij}}. \tag{2}$$

To calculate the derivatives on the right hand side of equation (2), we introduce the following kinematic assumptions:

(i) the periodic directions of the lattice change according to the macroscopic displacement gradient;
(ii) the lattice remains periodic during deformation.

Table 1. Compatibility and periodic equilibrium conditions for the sample lattices: $\mathbf{G}$ is the displacement gradient; $\mathbf{a}_i$ are the periodic vectors defined in figure 3; $\mathbf{F}_i$ are the nodal displacements and are the nodal forces.

	Hexagonal lattice	Chevron lattice
Compatibility	$\mathbf{s}_3 = \mathbf{s}_2 + \mathbf{G}\mathbf{a}_1$	$\mathbf{s}_3 = \mathbf{s}_2 + \mathbf{G}\mathbf{a}_1$
	$\mathbf{s}_4 = \mathbf{s}_2 + \mathbf{G}\mathbf{a}_2$	$\mathbf{s}_6 = \mathbf{s}_2 + \mathbf{G}\mathbf{a}_2$
		$\mathbf{s}_7 = \mathbf{s}_4 + \mathbf{G}(\mathbf{a}_2 - \mathbf{a}_1)$
Periodic equilibrium	$\mathbf{F}_1 = 0$	$\mathbf{F}_1 = 0$
	$\mathbf{F}_1 + \mathbf{F}_2 + \mathbf{F}_4 = 0$	$\mathbf{F}_5 = 0$
		$\mathbf{F}_2 + \mathbf{F}_3 + \mathbf{F}_6 = 0$
		$\mathbf{F}_7 + \mathbf{F}_4 = 0$

We remark that assumption (i) applies only to the periodic directions; no further hypothesis restricts the displacement of the internal points of the RVE, whose configuration is determined by imposing equilibrium. To illustrate how the array $\frac{\partial \mathbf{s}}{\partial G_{ij}}$ is determined, consider, as an example, the lattices in figure 1(b).

As we can observe, assumption (i) introduces constraints among the displacement of the nodes located on the RVE boundary. We name them compatibility equations. Since these nodes are necessarily corresponding along the periodic vectors, their relative displacements are given by the deformation of the periodic directions. On the other hand from assumption (ii), we can write the equilibrium equations of the RVE, under the action of the surrounding elements. These equations are written in terms of the nodal forces of the prescribed RVE, and we name them periodic equilibrium conditions. With reference to the lattices in figure 3, the kinematic and the equilibrium conditions can be formulated as shown in table 1, where $\mathbf{a}_1$ and $\mathbf{a}_2$ are the periodic directions of the lattice.

As we can observe, the compatibility equations allow us to express the displacements of all the nodes of the RVE in terms of $\mathbf{G}$ and of the displacement of a subset of the nodes of the RVE, which we call independent nodes. A possible choice of the independent nodes are nodes 2 and 3 for the hexagonal lattice (figure 3(a)), and 1, 5, 2, and 7 for the chevron (figure 3(b)). Since the number of equilibrium equations is

always equal to the number of independent nodes, the problem is closed; given the components of the displacement gradient, we can then determine the corresponding configuration of the RVE. If no bifurcation point is present along the load path, such configuration is unique. More in general, it is possible to show (Vigliotti *et al* 2014) that the nodal displacement of the RVE, and the periodic equilibrium equations can be expressed as follow

$$\mathbf{s} = \mathbf{B}_0\bar{\mathbf{s}} + \mathbf{B}_G\mathbf{G}, \tag{3}$$

$$\mathbf{B}_0^T\mathbf{F}(\mathbf{s}) = 0, \tag{4}$$

where $\mathbf{B}_0$ and $\mathbf{G}$ are matrices that depend only on the topology and connectivity of the lattice. After substituting equation (3) in (4), and recalling the statement of the virtual work (2), we can obtain the following expression for the macroscopic stress tensor and its Jacobian:

$$\mathbf{P} = \frac{1}{V_{\mathrm{RVE}}}\mathbf{B}_G^T\mathbf{F}(\mathbf{s}), \tag{5}$$

$$\frac{\partial\mathbf{P}}{\partial\mathbf{G}} = \frac{1}{V_{\mathrm{RVE}}}\left(\mathbf{B}_0\frac{\partial\bar{\mathbf{s}}}{\partial\mathbf{G}} + \mathbf{B}_G\right)^T\frac{\partial\mathbf{F}}{\partial\mathbf{s}}\left(\mathbf{B}_0\frac{\partial\bar{\mathbf{s}}}{\partial\mathbf{G}} + \mathbf{B}_G\right), \tag{6}$$

where $\frac{\partial\bar{\mathbf{s}}}{\partial\mathbf{G}}$ is given by the equation that follows, and $()^+$ denotes the Moore–Penrose pseudo inverse.

$$\frac{\partial\bar{\mathbf{s}}}{\partial\mathbf{G}} = -\left(\mathbf{B}_0^T\frac{\partial\mathbf{F}}{\partial\mathbf{s}}\mathbf{B}_0\right)^+\mathbf{B}_0^T\frac{\partial\mathbf{F}}{\partial\mathbf{s}}\mathbf{B}_G. \tag{7}$$

The methodology described in this section permits to model a component in lattice material by means of displacement-based finite element analyses. For a displacement gradient $\mathbf{G}$, at each integration point of the macroscopic structure, equations (3) and (4) enable to find first the configuration of the RVE, and equations (5) and (6) can be used to evaluate the 1PK tensor and its Jacobian for any given $\mathbf{G}$.

In the formulation described above, all the boundary conditions are on the components of $\mathbf{G}$, which ensures the existence of a solution. Nonetheless it is also possible to pose the inverse problem, that is to consider boundary conditions given on the $\mathbf{P}$ tensor and solve for $\mathbf{G}$. In the following sections, we consider mixed boundary conditions, where certain components of $\mathbf{P}$ and $\mathbf{G}$ are prescribed and others are free. In this case, the solution can still be found by solving a nonlinear problem by means of the Newton–Rhapson method, which iterates on the not prescribed, components of $\mathbf{G}$, and defines the residual on the components of $\mathbf{G}$, whose values are constrained. In this case special, proper care should apply, as bifurcation points might appear due to the local buckling of the lattice elements.

4. Mechanical properties of skin panels in lattice material

This section presents a methodology to design lattice materials for skin panels undergoing large cord and curvature changes. As a reference case, a plate subject to the boundary conditions shown in figure 1(b) is considered; in this case the macroscopic strain and stress fields of the plate are uniform and given by[3]

$$G_{22} = \frac{\Delta L_Y}{L_Y} = \text{constant},$$
$$G_{11} = G_{21} = G_{21} = 0,$$
$$P_{33} = P_{23} = P_{32} = P_{13} = P_{31} = 0.$$

Since the skin panels of an aerofoil are essentially planar, and the morphing is limited to the plane of the skin, we focus on extruded lattices, as shown in figure 4. Via the method described in the previous section, the macroscopic constitutive relations can be obtained for any choice of lattice parameters and with the assumption that the properties of the solid material are given. We observe that the size of the lattice in direction X_3, coincides with the thickness of the skin panel and is thus a macroscopic parameter; on the other hand, the in-plane dimensions of the lattice, i.e. the length and the thickness of its elements, are microscopic parameters, specified at a length scale smaller than the macroscopic dimension of the panel. With reference to figure 4, let L_i be the typical length of the walls in the plane of the plate, t be the wall thickness in the same plane, and z be the out of plane height of the walls corresponding to the macroscopic thickness of the plate. For these conditions, we assume the following relation holds: $t \ll L_i \ll z$. In the present study, the lattice walls are modelled as three-dimensional plates; thus for the macroscopic deformation modes that remain in the plane of the skin panel, the strain energy is essentially stored as pure bending in the walls, whereas for the deformation modes out of the plane $X_1 - X_2$, which correspond to the macroscopic bending of the plate, the strain energy is stored as membrane shear in the walls.

An essential parameter of a morphing skin panel is its bending stiffness, which is proportional to the thickness of the plate. As an indicator of the macroscopic bending stiffness of a skin plate made of a lattice material, we select the macroscopic shear stiffness of the lattice in the direction out of the plane $X_1 - X_2$, that is we consider the components of the macroscopic material stiffness tensor, equation (6), such that $\frac{\partial P_{31}}{\partial G_{3j}}$ with $i, j \in \{1, 2\}$.

We remark that in the design of a morphing skin panel we are mainly interested in the actuation forces necessary to obtain a given deformation per a unit surface of the panel. In the context of this paper, instead of comparing skin panels of given thickness, we compare panels for given bending stiffness, a key requirement to design a morphing wing panel. For each lattice, we consider a reference macroscopic thickness of the skin in the X_3 direction, $\bar{z}$, such that the following holds $\frac{1}{E_s}\frac{\partial P_{31}}{\partial G_{3j}}\frac{\bar{z}}{L_1} = \overline{\chi}^* = 1 \times 10^{-6}$, where E_s is the Young's modulus of the solid material.

In addition, as a measure of the actuation forces, and of the actuation work, in the sections that follow we consider the quantities $P_{11}^* = \frac{P_{11}}{E_s}\frac{\bar{z}}{L_1}$ and $P_{22}^* = \frac{P_{22}}{E_s}\frac{\bar{z}}{L_1}$. We note that since L_1 is

[3] We recall that the displacement gradient and the 1PK tensor are not symmetric, thus $G_{ij} \neq G_{ji}$ and $P_{ij} \neq P_{ji}$.

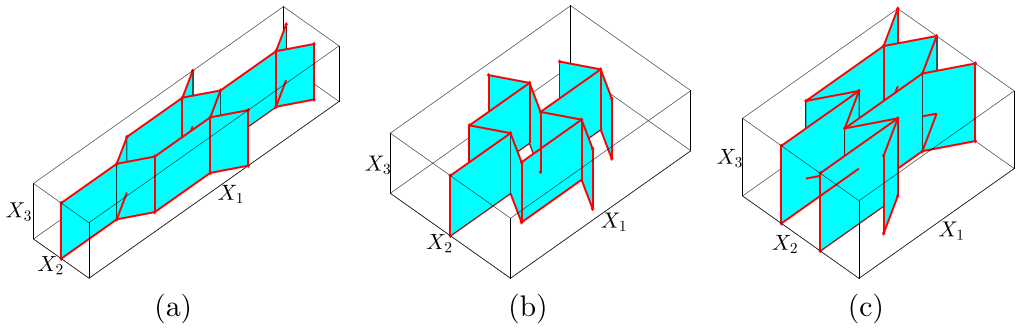

Figure 4. Sample lattices: (a) classical hexagonal lattice, (b) auxetic hexagonal lattice, (c) chevron lattice. We observe that the lattices with auxetic behaviour are obtained from classic honeycombs by letting $\phi \in]\pi/2, \pi[$. We also observe that the two hexagonal configurations coexist in the chevron lattice.

Table 2. Initial stiffness terms normalized with respect to the Young modulus, E_s, of the solid material.

	$\frac{\partial P_{22}}{\partial G_{22}}\frac{1}{E_s}$ $P_1 = 0$	$\frac{\partial P_{22}}{\partial G_{22}}\frac{1}{E_s}$ $G_{11} = 0$	$\frac{\partial P_1}{\partial G_{22}}\frac{1}{E_s}$ $G_{11} = 0$	$\frac{\partial P_{32}}{\partial G_{32}}\frac{1}{E_s}$ $G_{11} = 0$	$\frac{\partial P_{31}}{\partial G_{31}}\frac{1}{E_s}$ $G_{11} = 0$
Classical hexagonal	2.30×10^{-6}	8.25×10^{-4}	8.17×10^{-2}	8.88×10^{-3}	1.48×10^{-2}
Classical hexagonal	2.28×10^{-5}	1.64×10^{-2}	-1.63×10^{-2}	2.94×10^{-2}	4.47×10^{-3}
Chevron	3.29×10^{-6}	3.29×10^{-6}	0	2.05×10^{-2}	6.41×10^{-3}

a prescribed quantity for the lattices examined in this study, the quantity P^*_{ij} is an actual adimensional measure of the actuation tension for panels of given shear stiffness. P^*_{ij} allows to calculate the effective compliance of the panel for the actuation deformation mode among configurations featuring a given shear stiffness. In addition, we observe that with the above definition of P^*_{ij}, the actuation energy per unit surface of the skin panel is given by the following

$$W = E_s \bar{z} \int P^*_{22}\, \mathrm{d}G_{22}.$$

Following the reasoning above, we define the effective relative density of the skin panel as $\rho^* = \rho\frac{\bar{z}}{L_1}$ where ρ is the geometric relative density of the material, defined as the ratio between the volume occupied by the solid material and the volume of the RVE. ρ^* is a quantity governed both by the geometric and elastic parameters of the unit cell only, whereas the term $\frac{\bar{z}}{L_1}$ introduces a correction that accounts for the shear stiffness of the lattice material. Finally, we observe that the quantity ρ^* is such that the volume of the solid material per unit surface of the skin panel is given by $\rho^* L_1$.

4.1. Analysis of selected lattice topologies

In this section we compare the mechanical responses of the topologies shown in figure 4 under uniaxial stretching. The linear elastic properties of the hexagonal lattices, in both classic and auxetic configuration, were studied in detail in Olympio and Gandhi (2010b), who expressed the macroscopic stiffness as a function of the lattice geometry. In their study, a family of lattice topologies, named accordion, were suggested. This family includes, as substructure, both auxetic and non-auexctic honeycomb unit cells, resulting in zero initial macroscopic Poisson ratio. The chevron topology analysed here presents a similar feature, as it includes two sections with equal Poisson's ratio but opposite sign. This topology has been also studied in (Douglas *et al* 2014) in the context of expandable vascular stent, and it was recognized as particularly suitable for the cases where large uniaxial deformations are required. In their study the authors isolated an RVE of the stent and analysed the stress distribution with focus on the formation of plastic hinges, which allow the stent to retain its shape after expansion. In this study, on the other hand, we derive the macroscopic constitutive relations for the lattices in figure 4 including the nonlinear response caused by the finite displacements of the lattice elements. We assume the solid material remains linear, since we require all deformations to be completely recoverable. We will show that under a large stretching, a lattice with zero macroscopic Poisson's ratio in the reference configuration, e.g. the chevron lattice (figure 4(c)), can hold elastic instabilities, which perturb the lattice equilibrium and cause the loss of their neutrality.

For all the lattices analysed in this section, we assume: $L_1 = 10^{-3}$ m, $L_2/L_1 = 0.5$, $E_s = 70$ GPa, $L_1/t = 30$. Table 2 reports their stiffness in the initial configuration for alternative macroscopic constraint conditions. The first column of the table shows the lattice stiffness in direction X_2 for uniaxial stress conditions, i.e. the lattice is free to deform in the other directions upon a deformation applied in direction X_2. As we can observe, each lattice has a very small stiffness, similar in value. The second column of the table reports the pertinent stiffness under planar uniaxial strain conditions, i.e. the lattice

deformation in direction X_1 is prevented, if the deformation is applied in direction X_2 and the lattice is not constrained in direction X_3. As we can observe, in these conditions the hexagonal lattices are two to three orders of magnitude stiffer, whereas the stiffness of the chevron lattice is unchanged. In particular, the initial Poisson's ratio of the chevron lattice is zero, which leads to the decoupling of the loads in the directions X_1 and X_2. In contrast for the hexagonal lattices, the Poisson's ratio has a finite value, which prevents deformation in direction X_1 and brings an increase in the lattice stiffness. The third column of the table reports the direct cross term for the plane $X_1 - X_2$ of the initial material stiffness matrix, i.e. the marginal stress increment in direction X_1 corresponding to the deformation in direction X_2. This term is an effective measure of the coupling between the directions X_1 and X_2 for a uniaxial stretch of the lattice. For the hexagonal lattices, this term has a value of the same order of magnitude, or larger, of that of the direct stiffness in direction X_2. On the other hand, it is zero for the chevron lattice, where the direction X_1 and X_2 are decoupled. Finally, the last two columns in table 2 report the macroscopic shear stiffness of the lattice for deformation out of the plane $X_1 - X_2$; they represent the bending stiffness of the skin panel.

To compare the skin properties for given bending stiffness, we first evaluate the homogenized out of plane shear stiffness of the lattice material for each configuration as $\chi = \min\left(\frac{\partial P_{i3}}{\partial G_{j3}}, \frac{\partial P_{3j}}{\partial G_{3j}}\right)$ with $i, j \in \{1, 2\}$; then we choose a skin thickness, $\bar{z}$, such that $\frac{\chi}{E_s}\frac{\bar{z}}{L_1} = \chi^*$. As shown in figures 5(a) and (b), the hexagonal lattice in both the configurations is very compliant for uniaxial stress, but rather stiff for uniaxial stretch. We also observe that the reaction force in the directions orthogonal to the applied stretch, has the same order of magnitude of the applied tension, or larger, for the case of the classical hexagon. In addition, we remark that for stretching above 20%, simulations could not be carried out further, due to appearance of catastrophic collapse modes in some lattice struts, subjected to high compressive forces. On the other hand, the chevron lattice is very compliant with reaction tensions essentially negligible even for very large deformation. Hence for a morphing wing skin, cell topologies that are particularly promising have an architecture (within the RVE) that features subsections with both negative and positive Poissons ratio, such as the chevron lattice.

5. Design space of the chevron lattice

In this section, we analyse the shear response of the chevron lattice in different configurations and plot its design space for given geometric parameters. In particular, we let the ratio between the horizontal and the inclined members vary in the range $L_2/L_1 \in [0.25, 4]$. To do so we keep L_1 constant, and we consider two values of the initial angle between the members, namely $\phi = 15°$ and $\phi = 30°$. Figure 6(a) shows the plot of the shear stiffness of the plate, $\chi = \min\left(\frac{\partial P_{13}}{\partial G_{13}}, \frac{\partial P_{23}}{\partial G_{23}}\right)$, for unit plate thickness, i.e. before the homogenization correction. As we can observe for small value of L_2/L_1, the stiffness of the material is dominated by the length of the horizontal member and it is constant. For larger values of L_2/L_1, as the length of the inclined member increases, the lattice becomes increasingly compliant for the out of plane shear in direction 2, and the overall shear stiffness of the plate decreases. As a result, the reference thickness of the skin increases to ensure the normalized macroscopic bending stiffness of the plate to be constant and equal to χ^*. Figure 6(b) shows the plot of the geometric relative density of the lattice material, and figure 6(c) shows the effective relative density of the plate, which includes the correction for the thickness of the plate, as dictated by the shear stiffness. As we can observe, even if the geometric relative density of the lattice material decreases for an increase of the aspect ratio of the unit cell (figure 6(b)), the effective relative density of the skin material (figure 6(b)) raises. The reason for this is that to increase the panel thickness is necessary to compensate the reduction of the macroscopic shear stiffness (figure 6(a)). It is also interesting to observe in figure 6(c) the merging of the curves for $\phi = 15°$ and $\phi = 30°$ after a certain value of L_2/L_1. In particular above $L_2/L_1 \approx 3$ and regardless of ϕ, the combined variations of shear stiffness and relative density reach a given value of the effective relative density.

Figures 7(a) and 8(a) show the normalized actuation tension required to obtain a 40% uniaxial deformation of the skin, respectively in extension and in compression. The chevron lattice becomes progressively compliant for higher L_2/L_1, since the bending stiffness of the inclined member decreases for longer length, L_2. In addition, lower values of the shear stiffness are obtained for lattices with higher L_2, a trend indicating that χ^* can remain constant only if the skin thickness increases. As a result, the net actuation force increases. Whereas this response is more evident for $\phi = 30°$, an increment is also observed for the case of $\phi = 15°$.

Figures 7(b) and 8(b) show the ratio between the applied force, P_{22}, and the reaction force in direction 1, at 40% deformation in extension and in compression respectively. For small values of L_2/L_1, the reaction forces are negligible both for $\phi = 30°$ and $\phi = 15°$. Yet, with the increase of the slenderness of the inclined members, the equilibrium at the joints between the horizontal and the inclined members becomes unstable; hence, a bifurcation point appears to allow joint rotation. As a result, inclined members experience a rise of bending moments, which in turn produce reaction forces in the direction orthogonal to that of the applied deformation, thereby leading to a loss of the lattice neutrality.

Figure 9 shows the curves of the tension deformation along with the deformed shape of the lattice for the case $L_2/L_1 = 4.0$. The development of instabilities in a lattice subject to macroscopically tensile loads, as a result of small misalignments, or deviations, from equilibrium, is an interesting case, identified and described in detail by Zaccaria *et al* (2011); Bigoni *et al* (2012). In the case $\phi = 30°$, bifurcation occurs for smaller values of L_2/L_1, whereas the ratio P_{11}/P_{22} reaches lower values than those for $\phi = 15°$, for which is between 4 and 5. Figures 7(c) and 8(c) show the maximum

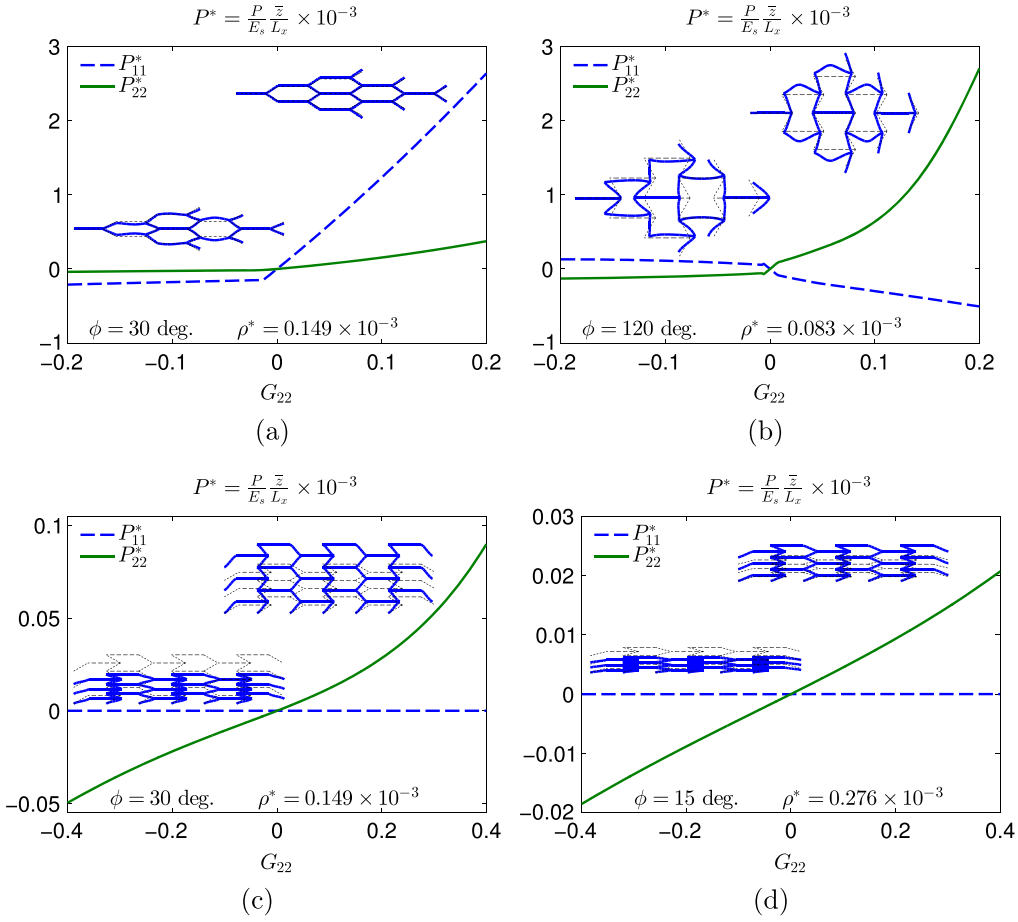

Figure 5. Normalized stress–strain relations for the lattices under investigation. Each plot includes the deformed shape of the RVE in compression and in tension for the largest value of the deformation. For each topology, the value of the tension has been evaluated for configurations where the skin thickness, z, yields in direction 3 a given shear macroscopic stiffness, given by $\chi = \min\left(\frac{\partial P_{i3}}{\partial G_{j3}}, \frac{\partial P_{3i}}{\partial G_{3j}}\right)$ with $i, j \in \{1, 2\}$. This metrics allows us to compare the effective actuation power, as given by the area under the P^*_{22} curve, for skin panels under a prescribed bending stiffness.

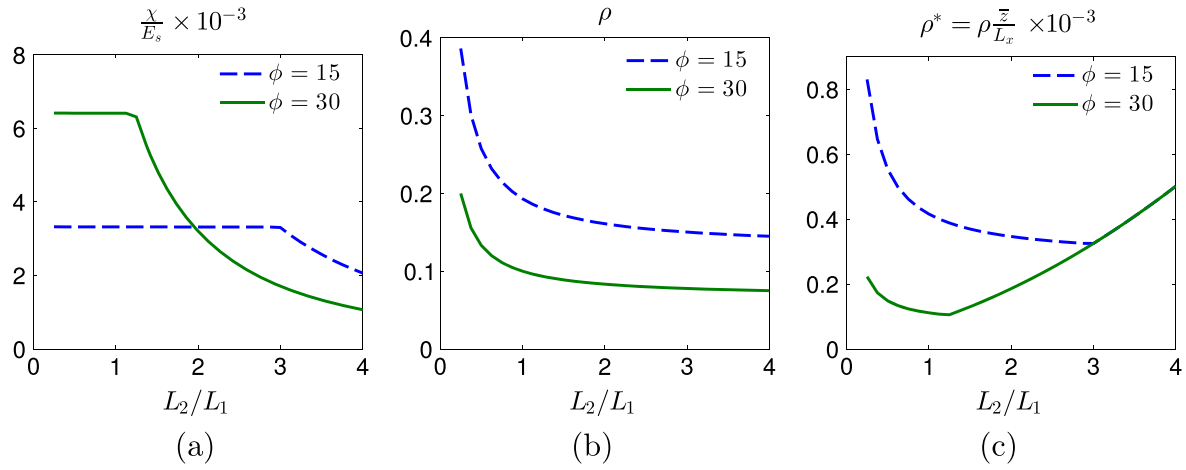

Figure 6. Shear stiffness and normalized relative density for given parameters of the chevron lattice. $\chi = \min\left(\frac{\partial P_{13}}{\partial G_{13}}, \frac{\partial P_{23}}{\partial G_{23}}\right)$ is the minimum out of plane shear stiffness of the material; ρ is the geometric relative density of the material, ρ^* is the effective relative density corrected to account for the material shear stiffness.

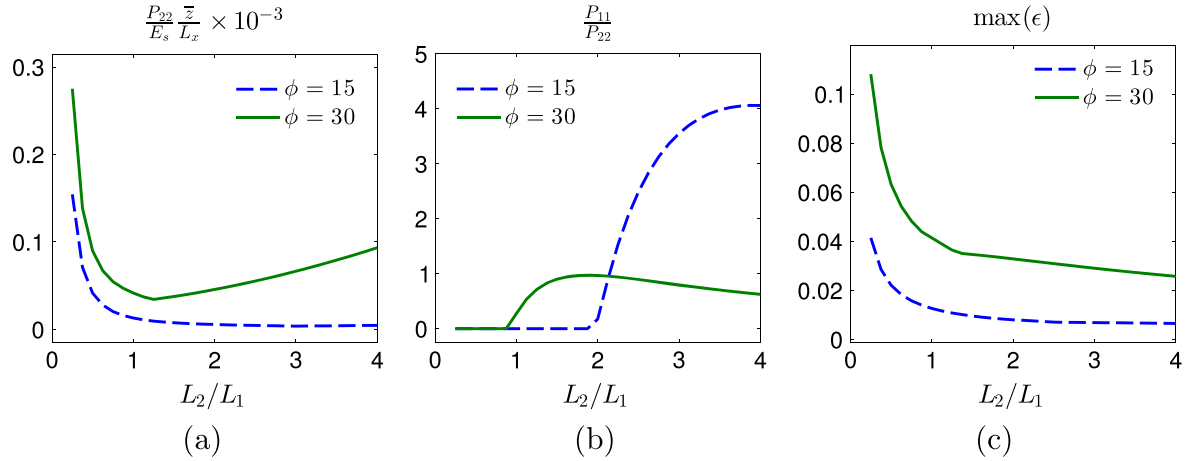

Figure 7. Normalized actuation stress, actuation ratio and maximum deformation of the solid material under tensile macroscopic applied strain. Curves obtained for different parameters of the chevron lattice for an actuation corresponding to 40% tension.

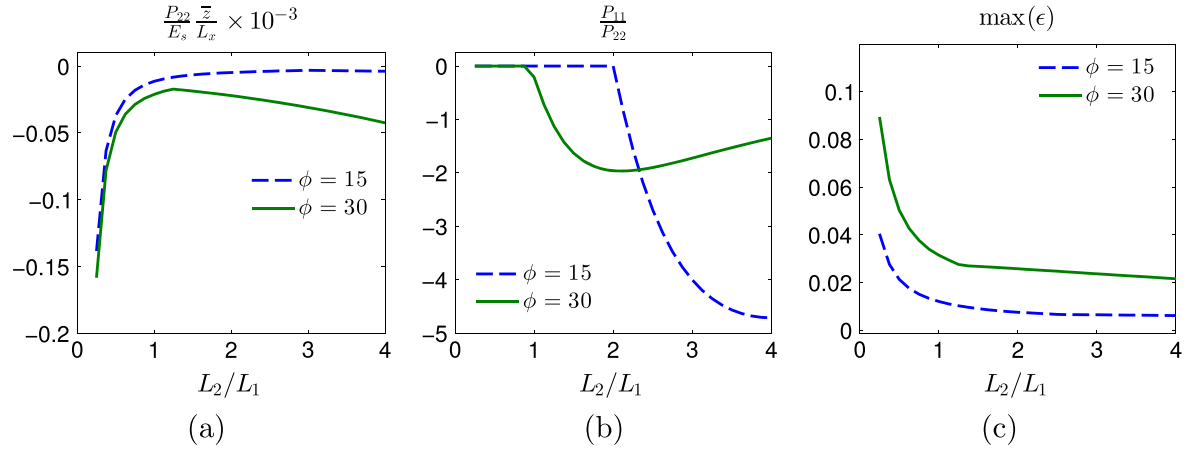

Figure 8. Normalized actuation stress, actuation ratio and maximum deformation of the solid material under compressive macroscopic applied strain. Curves obtained for different parameters of the chevron lattice for an actuation corresponding to 40% compression.

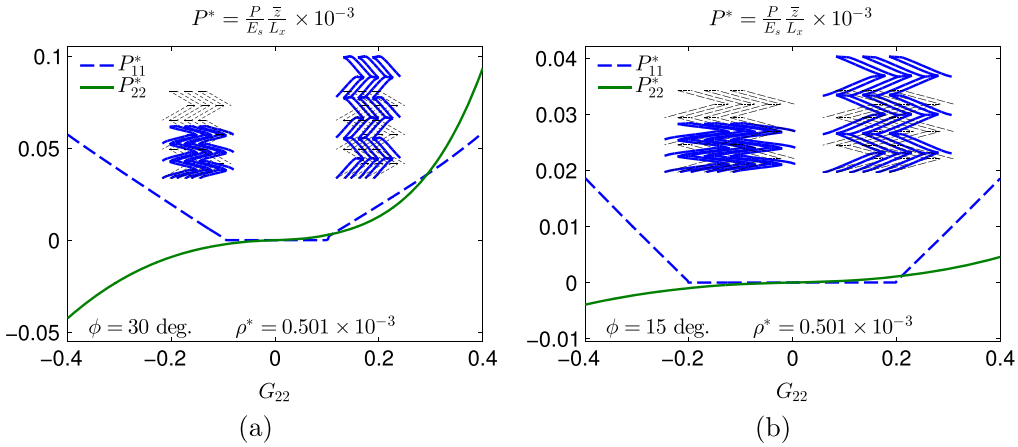

Figure 9. Normalised stress/strain relation for selected lattices for the case $L_2/L_1 = 4.0$. Each plot includes the deformed shape of the RVE in compression and in tension for the largest value of the deformation. The picture shows the occurrence of structural instabilities in a lattice subject to macroscopically tensile loads, as a result of small misalignments during loading.

nominal deformation in the solid material of the lattice. This quantity specifies the allowable limit for the macroscopic deformation of the skin, and it should be compared with the elastic limit of the material of the lattice. The figures show that the microstructure of the lattice is very effective in translating in plane stretches into bending and large rotation of the lattice members that keep actuation forces and solid material deformation quite low. In addition, the lattice can

yield macroscopic deformation in the order of 40%, while limiting the microscopic deformation of the material below 5%.

For the material choice of a morphing wing skin, there is no single best that meets the design specifications; rather, an optimal solution is to be found from case to case. In fact, large values of L_2/L_1 ensure low actuation tension and small strain in the solid material (see figures 7(a), (c) and 8(a), (c)). On the other hand, these values also produce an heavier skin and larger forces in the transverse direction, an outcome that calls for a stronger and heavier wing-box structure. Furthermore, there is no ideal angle for the inclined members; lower values of ϕ increase compliance, but heavier lattices or stronger coupling between the actuation and the constraint directions are possible by controlling the value of L_2/L_1. In general, the final concept design for a lattice skin needs to take into account the actual properties of the solid material, the overall geometric dimensions of the wing, and the strength of the structure surrounding the morphing flap. An approach to find trade-off lattice concepts can be developed in a future work to optimally reconcile the conflicting requirements of a morphing wing skin.

6. Conclusions

In this paper, we use a homogenization method to analyse the mechanical properties of a lattice morphing skin undergoing large deformation. As reference cases, we examined the properties of hexagonal honeycombs, both in the classical and in the auxetic configuration, and the properties of a chevron lattice. We have shown that the chevron lattice is capable to maintain high compliance in the actuation direction; in addition for large actuation strokes, the chevron lattice can keep the deformation in the actuation direction decoupled from the deformation in the in-plane orthogonal direction. The multiscale method used here has enabled to formulate macroscopic constitutive relations of the lattices, and to appraise the performance limits for a range of the lattice parameters. Capable to account for the geometrical non-linearities induced by finite strains, the method allows to identify the occurrence of static instability even in lattices macroscopically subjected to tensile external loads. The method also enables to predict the macroscopic response of a given lattice from the analysis of a uniform medium; hence, it can be readily integrated within an optimization framework that includes a model of the entire wing.

Acknowledgments

Andrea Vigliotti would like to acknowledge the Royal Society for the support received through the Newton International Fellowship.

References

Arabnejad S and Pasini D 2013 Mechanical properties of lattice materials via asymptotic homogenization and comparison with alternative homogenization methods *Int. J. Mech. Sci.* **77** 249–62

Barbarino S, Bilgen O, Ajaj R M, Friswell M I and Inman D J 2011 A review of morphing aircraft *J. Intell. Mater. Syst. Struct.* **22** 823–77

Barbarino S, Saavedra Flores E, Ajaj R, Dayyani I and Friswell M 2014 A review on shape memory alloys with applications to morphing aircraft *Smart Mater. Struct.* **23** 063001

Bigoni D, Misseroni D, Noselli G and Zaccaria D 2012 Effects of the constraint's curvature on structural instability: tensile buckling and multiple bifurcations *Proc. R. Soc.* A **468** 2191–209

Chen Y, Scarpa F, Farrow I, Liu Y and Leng J 2013 Composite flexible skin with large negative Poisson's ratio range: numerical and experimental analysis *Smart Mater. Struct.* **22** 045005

Daynes S and Weaver P 2012 Design and testing of a deformable wind turbine blade control surface *Smart Mater. Struct.* **21**

Dayyani I, Ziaei-Rad S and Friswell M 2014 The mechanical behaviour of composite corrugated core coated with elastomer for morphing skins *J. Compos. Mater.* **48** 1623–36

Deshpande V S, Ashby M F and Fleck N A 2001 Foam topology: bending versus stretching dominated architectures *Acta Mater.* **49** 1035–40

Douglas G, Phani A and Gagnon J 2014 Analyses and design of expansion mechanisms of balloon expandable vascular stents *J. Biomech.* **47** 1438–46

Gibson L and Ashby M 1982 Mechanics of three-dimensional cellular materials *Proc. R. Soc.* A **382** 43–59

Gibson L J, Ashby M F, Schajer G S and Robertson C I 1982 The mechanics of two-dimensional cellular materials *Proc. R. Soc.* A **382** 25–42

Gomez J and Garcia E 2011 Morphing unmanned aerial vehicles *Smart Mater. Struct.* **20** 103001

Hengsbach S and Lantada A 2014 Direct laser writing of auxetic structures: present capabilities and challenges *Smart Mater. Struct.* **23** 085033

Kuder I, Arrieta A, Raither W and Ermanni P 2013 Variable stiffness material and structural concepts for morphing applications *Prog. Aerosp. Sci.* **63** 33–55

Noor A K 1988 Continuum modeling for repetitive lattice structures *Appl. Mech. Rev.* **41** 285–96

Olympio K and Gandhi F 2010a Flexible skins for morphing aircraft using cellular honeycomb cores *J. Intell. Mater. Syst. Struct.* **21** 1719–35

Olympio K and Gandhi F 2010b Zero poisson's ratio cellular honeycombs for flex skins undergoing one-dimensional morphing *J. Intell. Mater. Syst. Struct.* **21** 1737–53

Olympio K, Gandhi F, Asheghian L and Kudva J 2010 Design of a flexible skin for a shear morphing wing *J. Intell. Mater. Syst. Struct.* **21** 1755–70

Ortona A, D'Angelo C, Gianella S and Gaia D 2012 Cellular ceramics produced by rapid prototyping and replication *Mater. Lett.* **80** 95–98

Previtali F and Ermanni P 2012 Performance of a non-tapered 3D morphing wing with integrated compliant ribs *Smart Mater. Struct.* **21** 055008

Raither W, Heymanns M, Bergamini A and Ermanni P 2013 Morphing wing structure with controllable twist based on adaptive bending-twist coupling *Smart Mater. Struct.* **22** 065017

Santer M and Pellegrino S 2009 Topological optimization of compliant adaptive wing structure *AIAA J.* **47** 523–34

Sofla A, Meguid S, Tan K and Yeo W 2010 Shape morphing of aircraft wing: status and challenges *Mater. Des.* **31** 1284–92

Spadoni A and Ruzzene M 2007 Static aeroelastic response of chiral-core airfoils *J. Intell. Mater. Syst. Struct.* **18** 1067–75
Stanewsky E 2001 Adaptive wing and flow control technology *Prog. Aerosp. Sci.* **37** 583–667
Thill C, Etches J, Bond I, Potter K and Weaver P 2008 Morphing skins *Aeronaut. J.* **112** 117–39
Thill C, Etches J, Bond I, Potter K and Weaver P 2010 Composite corrugated structures for morphing wing skin applications *Smart Mater. Struct.* **19** 124009
Vaezi M, Seitz H and Yang S 2013 A review on 3D micro-additive manufacturing technologies *Int. J. Adv. Manuf. Technol.* **67** 1721–54
Vigliotti A, Deshpande V and Pasini D 2014 Nonlinear constitutive models for lattice materials *J. Mech. Phys. Solids* **64** 44–60
Vigliotti A and Pasini D 2012a Linear multiscale analysis and finite element validation of stretching and bending dominated lattice materials *Mech. Mater.* **46** 57–68
Vigliotti A and Pasini D 2012b Stiffness and strength of tridimensional periodic lattices *Comput. Methods Appl. Mech. Eng.* **229-232** 27–43
Wereley N and Gandhi F 2010 Flexible skins for morphing aircraft *J. Intell. Mater. Syst. Struct.* **21** 1697–8
Wlezien R W, Horner G C, McGowan A R, Padula S L, Scott M A, Silcox R J and Simpson J O 1998 The aircraft morphing program *Technical Report* NASA Langley doi:10.1177/1045389X10393157
Zaccaria D, Bigoni D, Noselli G and Misseroni D 2011 Structures buckling under tensile dead load *Proc. R. Soc.* A **467** 1686–700